

Pulsed ENDOR Studies of Short-Lived Spin-Correlated Radical Pairs in Photosynthetic Reaction Centers

Catherine E. Fursman, Christian Teutloff, and Robert Bittl^{*,†}

Max-Volmer-Laboratorium, Technische Universität Berlin, Strasse des 17. Juni 135, 10623 Berlin, Germany

Received: March 5, 2002; In Final Form: June 13, 2002

Time-resolved electron–nuclear double resonance (TR-ENDOR) performed on the spin-correlated radical pair $P_{700}^+ A_1^-$ in frozen solution samples of PSI shows a superposition of the ENDOR lines expected for the individual radicals P_{700}^+ and A_1^- . Presented here are TR-ENDOR spectra taken over a range of EPR field positions. The spectra are unusual because they show both absorptive and emissive contributions and a strong dependence on the field. The nature of the spectra is explored using the theory of spin-correlated radical pairs. It is found that the electron spin polarization in the radical pair is responsible for the absorptive/emissive nature of the TR-ENDOR spectra and that the mixed electronic eigenstates give rise to transitions in addition to those usually found in ENDOR. Computer simulations based on a model containing two coupled electrons and a single spin- $1/2$ nucleus are able to reproduce the spectra and their field dependence. It is also shown that TR-ENDOR spectra from a spin-correlated radical pair are sensitive to the relative signs of the hyperfine couplings.

1. Introduction

The transmembrane protein complex photosystem I (PSI) is part of the photosynthetic apparatus in oxygen-evolving species such as green plants and cyanobacteria. The 3D structure of PSI was recently resolved to 2.5 Å.¹ The fundamental process occurring within PSI is electron transfer (ET) between cofactors of the reaction center (RC), which leads to a charge separation across the membrane. The cofactors involved in the ET comprise a chlorophyll dimer P_{700} , a monomer A_0 , a phylloquinone A_1 , and three iron–sulfur clusters F_X , F_A , and F_B . ET in PSI is initiated when P_{700} is excited either by excitation energy transfer from antenna chlorophylls or by direct absorption of a photon. The excited singlet state P_{700}^* rapidly passes an electron to the primary acceptor A_0 . The electron is subsequently transferred, via the secondary acceptor A_1 , through the chain of Fe–S clusters. This process in PSI is the subject of a recent review.² Paramagnetic states of most of these cofactors have been studied extensively using continuous wave (CW) EPR and electron–nuclear double resonance (ENDOR) spectroscopy in both frozen solution samples and single crystals. This work is the subject of several recent reviews.^{3–6}

The species to be investigated is generally trapped by selective photoaccumulation, which sometimes involves the use of redox reagents. However, some of the paramagnetic species arising during the ET in PSI can also be studied in their natural states. An example is the short-lived radical pair $P_{700}^+ A_1^-$. This state is formed from a molecular singlet precursor in a spin-correlated state and is spin polarized. At physiological temperatures, $P_{700}^+ A_1^-$ has a lifetime of about 200 ns. At temperatures lower than 200 K, around 70% of PSI reaction centers in *Synechococcus elongatus* undergo a cyclic electron transfer⁷ that creates $P_{700}^+ A_1^-$ with a lifetime of about 100 μ s. The remaining 30%

undergo an irreversible charge separation to create $P_{700}^+ F_B^-$. Using transient EPR, $P_{700}^+ A_1^-$ can be investigated at both physiological and cryogenic temperatures. Results of these studies have recently been reviewed.⁸ In the low-temperature case, the lifetime is long enough for $P_{700}^+ A_1^-$ to be studied by pulsed time-resolved (TR)-EPR methods such as the field-swept echo (FSE) experiment and out-of-phase electron spin–echo envelope modulation (OOP-ESEEM) spectroscopy.^{9–11} When applied to frozen solution samples of PSI, OOP-ESEEM can be used to determine the magnitudes of the spin–spin interactions between P_{700}^+ and A_1^- and hence the distance between them, as reviewed recently.¹²

Single-crystal EPR studies on paramagnetic intermediates in PSI are used to determine not only the principal values of the magnetic interaction parameters but also the orientation of the principal axes with respect to the crystal structure, yielding spatial information about the reaction center.^{13,14} ENDOR on single crystals¹⁵ of P_{700}^+ in PSI determined the orientation of the hyperfine tensors within the crystal. This could in principle aid, for example, the assignment of hydrogen bonds. This information has so far not been available for A_1^- ; it is not possible to perform single-crystal measurements on the photoaccumulated phylloquinone in PSI because the required procedure destroys the crystal structure. However, in principle, single-crystal TR-ENDOR experiments performed on the radical pair $P_{700}^+ A_1^-$ could yield this information.

TR-ENDOR experiments^{16,17} on $P_{700}^+ A_1^-$ in a frozen solution sample of PSI from *S. elongatus* have given spectra that are a superposition of the ENDOR spectra of P_{700}^+ and A_1^- . However, TR-ENDOR spectra are rather complex and need to be analyzed in detail before the experiment can be applied usefully to single crystals. The analysis of TR-ENDOR spectra given here uses the model of spin-correlated radical pairs (SCRPs).^{18,19} Important ingredients of this model are the generation of radical pairs in a pure spin state (the singlet state in the case of photosystems) and the presence of electron spin–

* Corresponding author. E-mail: robert.bittl@physik.fu-berlin.de. Fax: +49 30 838-56046.

[†] New address: Fachbereich Physik, Freie Universität Berlin, Arnimallee 14, 14195 Berlin, Germany.

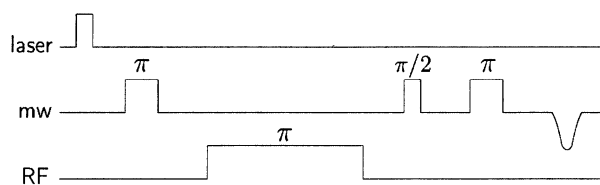


Figure 1. Pulse sequence for time-resolved ENDOR on transient light-induced radical pair states. The laser pulse is applied 500 ns before the inversion pulse at the start of a Davies-type ENDOR pulse sequence, with pulse lengths of $\tau_{mw} = 128$ ns and $\tau_{RF} = 8$ μ s. The period between the first and second mw pulses was 11 μ s. During the detection sequence ($\pi/2_{mw} - \tau - \pi_{mw} - \tau$ - echo), the interpulse delay τ was 600 ns.

spin coupling during observation. TR-EPR spectra of radical pairs in photosynthesis can be successfully described using the SCRP concept²⁰ and yield valuable structural information (for a review, see ref 8). In contrast to the case of radical pairs and biradicals in liquid solution where the hyperfine interaction is often resolved in TR-EPR spectra (see, for example, ref 19), the TR-EPR spectra of radical pairs in photosynthesis usually show no hyperfine resolution. Consequently, in the latter case, the hyperfine interaction is considered in spectra simulations to be only a source of inhomogeneous broadening. Therefore, to resolve the hyperfine interaction under these circumstances, TR-ENDOR is necessary. The purpose of this paper is to present a set of TR-ENDOR spectra obtained over a range of field positions from $P_{700}^+ A_1^-$ and to provide a qualitative explanation of the significant features of the spectra. In general, each spectrum exhibits both absorptive (A) and emissive (E) ENDOR lines, with the quantity of A and E character in each being strongly field-dependent. These effects and effects of the sign of the hyperfine coupling (hfc) are explained here on the basis of the SCRP^{18,19} concept. We conclude that small differences in the positions of spectral features between stationary and TR-ENDOR experiments are not due to differences in the types of experiments but are likely caused by differences in the local environment of the radicals in both experiments.

2. Experimental Methods

TR-ENDOR was performed on PSI reaction-center samples prepared as described²¹ and frozen in the dark with 30–50 mM sodium ascorbate to keep P_{700} in the neutral state. Measurements were taken on a Bruker ESP380E with an ESP360D-P accessory. The sample was helium-cooled to 80 K with an Oxford CF935 cryostat. Light excitation was achieved with pulses from a Nd:YAG laser (Spectra Physics GCR 130) with $\lambda = 532$ nm, an 8-ns pulse width, and a repetition rate of 10 Hz. The laser flash was applied 500 ns prior to the first microwave (mw) pulse, creating $P_{700}^+ A_1^-$ and allowing the zero quantum coherence^{9,22,23} to dephase^{24–26} before the application of the usual Davies-type ENDOR sequence,²⁷ as shown in Figure 1.

3. Results and Discussion

3.1. Experimental Results. A Davies ENDOR spectrum from A_1^- in PSI from *S. elongatus* is shown in Figure 2, where it is compared with a TR-ENDOR spectrum taken from $P_{700}^+ A_1^-$. The two spectra have quite similar main features; both contain a pronounced axially symmetric hyperfine tensor and a coupling (*) at the edge of the matrix region. In this work, we concentrate only on these particular features of the ENDOR spectra, both of which are due to A_1^- ; couplings from P_{700}^+ are superimposed only in the central region of the TR-ENDOR spectrum and in general give much weaker signals.

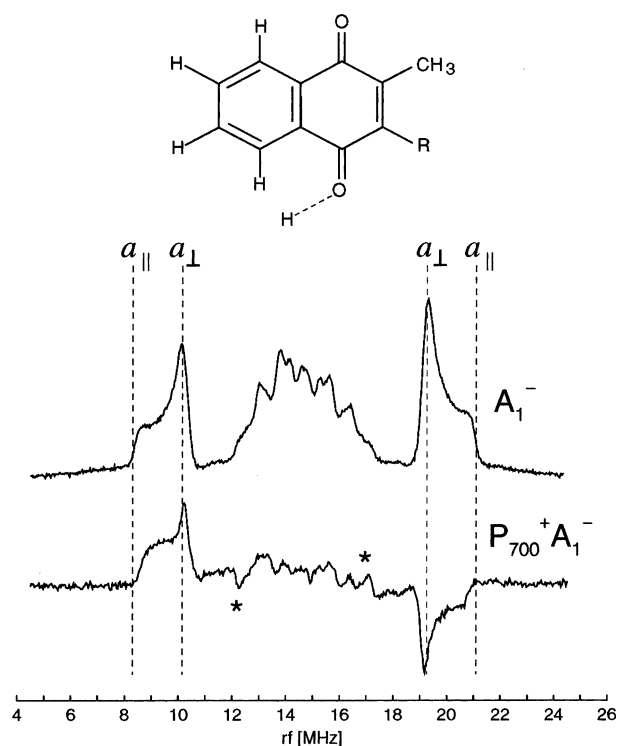


Figure 2. Structure of the phyloquinone and Davies ENDOR spectra of A_1^- and $P_{700}^+ A_1^-$ both from PSI in *S. elongatus* taken at 80 K. Also marked are the positions of the principal values of the axial hyperfine coupling in A_1^- and the smaller coupling from $P_{700}^+ A_1^-$ (*).

The axial hfc has previously been seen in CW²⁸ and pulsed²⁹ ENDOR studies on photoaccumulated A_1^- and in CW EPR spectra taken at X-, Q-, and W-bands,³⁰ in which it is partially resolved. The coupling is assigned to the phyloquinone methyl group (see Figure 2). In alkaline ethanol *in vitro*, the principal values of this hfc were measured²⁸ as $a_{||} = 10.0$ MHz and $a_{\perp} = 6.8$ MHz. In both spectra shown in Figure 2, these principal values are increased: for photoaccumulated A_1^- , $a_{||} = 12.8$ MHz and $a_{\perp} = 9.1$ MHz, and for $P_{700}^+ A_1^-$, $a_{||} = 12.3$ MHz and $a_{\perp} = 8.8$ MHz. The increase in the hfc in both *in vivo* spectra is most likely due to interactions between A_1^- and the protein. Whether the shift in the $P_{700}^+ A_1^-$ spectra comes from the presence of the coupling between the electrons will be investigated here.

The most striking aspect of the TR-ENDOR spectrum is that it has both A and E contributions. A particular point of interest is that whereas the axial tensor from the methyl coupling has A/E character, the smaller coupling (*) has E/A character. This coupling is most likely due to either an α proton or to the hydrogen bond suggested by the X-ray structure¹ and shown in Figure 2. In either case, the hfc would have opposite sign to that of the methyl coupling, which suggests that TR-ENDOR from SCRPs is sensitive to the relative signs of the hfc's. This information is usually obtained only from a general-TRIPLE experiment³¹ performed in addition to ENDOR.

Figure 3 shows the field-swept echo spectrum (FSE) taken from $P_{700}^+ A_1^-$ and TR-ENDOR spectra taken at different field positions within the FSE. The TR-ENDOR spectra reveal that the A/E nature of the ENDOR lines is strongly field-dependent. At the low-field edge, where the FSE is emissive, the ENDOR lines are mainly in emission. Moving to higher magnetic field introduces absorptive peaks on the low-frequency side of the ENDOR spectra, all of which disappear as the high-field edge of the spectrum is approached. The unusual appearance of the

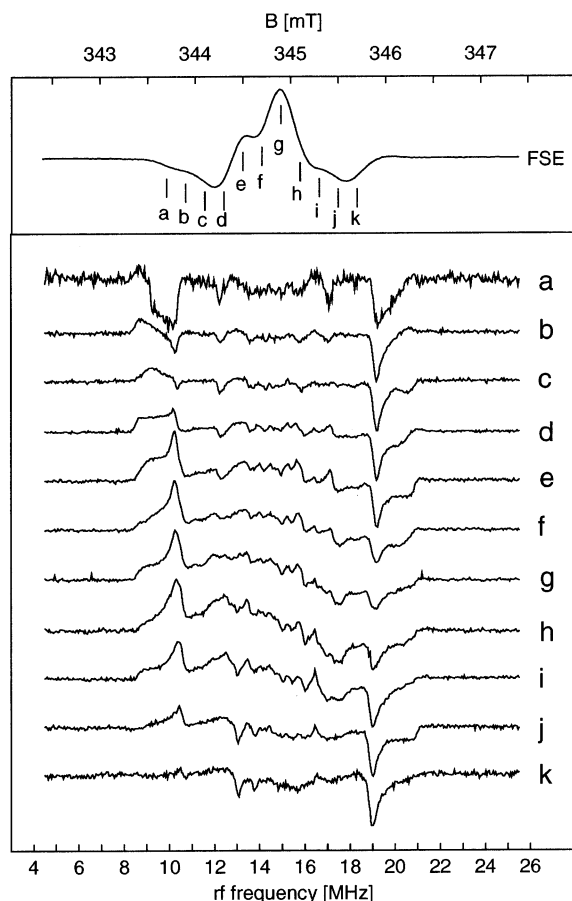


Figure 3. Field-swept echo (top) and TR-ENDOR spectra of $P_{700}^+ A_1^-$ in *S. elongatus* taken at 80 K. The respective field positions of the ENDOR spectra are indicated in the field-swept echo spectrum.

TR-ENDOR spectra from this SCRPs suggests that extra information, such as the relative signs of the hfc and the magnitudes of the spin–spin coupling constants, could be contained within them.

3.2. Theory. 3.2.1. Model for ENDOR on Radical Pairs.

The TR-ENDOR experiment on a radical-pair state such as $P_{700}^+ A_1^-$ can be explored through the use of the SCRPs model.^{19,22,32} In the following calculations, the system is approximated by a pair of spin–spin coupled electrons A and B (representing A_1^- and P_{700}^+ , respectively) and a spin- $1/2$ nucleus, N, which is coupled via an axial hyperfine interaction a to electron A. The electronic spin–spin coupling consists of a traceless axial dipolar tensor \mathbf{D} with z -component D_{zz} and isotropic exchange interaction J . The spin Hamiltonian for the system in the rotating frame is given in eq 1

$$\hat{\mathcal{H}}_0 = \omega_A \hat{S}_{Az} + \omega_B \hat{S}_{Bz} - 2J \hat{S}_A \hat{S}_B + D_{zz} (3\hat{S}_{Az} \hat{S}_{Bz} - \hat{S}_A \hat{S}_B) + a_{zz} \hat{S}_{Az} \hat{S}_{Nz} - \omega_N \hat{S}_{Nz} \quad (1)$$

where the ω_i values ($i = A, B, N$) are the Larmor frequencies of the spins.

The allowed EPR and ENDOR transitions within this system can be explored by consideration of the eigensystem that results from a diagonalization of the spin Hamiltonian. The radical pair was not assumed to be weakly coupled, and hence the nonsecular parts of D_{zz} and J were included. In contrast to some other work on SCRPs,^{33–35} this model neglects the pseudo-secular part of the hyperfine coupling, meaning that the nuclear spin states are not mixed. Thus, of the eight eigenstates, four describe states with an α -spin nucleus, and four describe states

with a β -spin nucleus. In the high-field approximation, the levels have the following energies:

$$\begin{aligned} E_{1\alpha} &= \omega + d + \frac{\omega_+}{2} & E_{1\beta} &= \omega + d - \frac{\omega_+}{2} \\ E_{2\alpha} &= -\frac{\omega_N}{2} - d + \frac{\Omega_\alpha}{2} & E_{2\beta} &= \frac{\omega_N}{2} - d + \frac{\Omega_\beta}{2} \\ E_{3\alpha} &= -\frac{\omega_N}{2} - d - \frac{\Omega_\alpha}{2} & E_{3\beta} &= \frac{\omega_N}{2} - d - \frac{\Omega_\beta}{2} \\ E_{4\alpha} &= -\omega + d - \frac{\omega_-}{2} & E_{4\beta} &= -\omega + d + \frac{\omega_-}{2} \end{aligned} \quad (2)$$

In eq 2, $\omega = (\omega_A + \omega_B)/2$, $d = (D_{zz} - J)/2$, and α and β refer to the spin states of the nucleus. In the singlet–triplet (ST) basis, the states have electronic character determined by

$$\begin{aligned} |1_\gamma\rangle &= |T_+\rangle \\ |2_\gamma\rangle &= \cos \psi_\gamma |S\rangle + \sin \psi_\gamma |T_0\rangle \\ |3_\gamma\rangle &= -\sin \psi_\gamma |S\rangle + \cos \psi_\gamma |T_0\rangle \\ |4_\gamma\rangle &= |T_-\rangle \end{aligned} \quad (3)$$

In the above equations, the singlet–triplet mixing angles ψ_α and ψ_β are defined (for $\gamma = \alpha$ or β) by

$$\sin 2\psi_\gamma = \frac{q_\gamma}{\Omega_\gamma} \quad \cos 2\psi_\gamma = \frac{j}{\Omega_\gamma} \quad \tan 2\psi_\gamma = \frac{q_\gamma}{j} \quad (4)$$

with

$$\Omega_\alpha = \sqrt{\left(\frac{a}{2} + q\right)^2 + j^2} \quad q_\alpha = \frac{a}{2} + q \quad (5)$$

$$\Omega_\beta = \sqrt{\left(\frac{a}{2} - q\right)^2 + j^2} \quad q_\beta = \frac{a}{2} - q \quad (6)$$

$j = D_{zz} + 2J$ and $q = \omega_A - \omega_B$. a is the effective hyperfine coupling (hfc). The pure triplet states $|1_\alpha\rangle$, $|1_\beta\rangle$, $|4_\alpha\rangle$, and $|4_\beta\rangle$ are dependent on either $\omega_+ = a/2 - \omega_N$ ($|T_+\rangle$ states) or $\omega_- = a/2 + \omega_N$ ($|T_-\rangle$ states). These expressions are the NMR frequencies of a spin- $1/2$ nucleus coupled to α - and β -electron spins, respectively. The energies of the states with both $|S\rangle$ and $|T_0\rangle$ character ($|2_\alpha\rangle$, $|2_\beta\rangle$, $|3_\alpha\rangle$, and $|3_\beta\rangle$) are dependent upon variations of these NMR frequencies and involve the terms Ω_α and Ω_β . A schematic representation of the eight energy levels of this three-spin system is given in Figure 4a. $P_{700}^+ A_1^-$ is formed from the singlet molecular precursor $P_{700}^* A_1$, and during the fast electron transfer via A_0 , the spin is conserved. Therefore, on creation, $P_{700}^+ A_1^-$ is also in a singlet state. The laser flash causes only those states with singlet character, namely, $|2_\alpha\rangle$, $|2_\beta\rangle$, $|3_\alpha\rangle$ and $|3_\beta\rangle$, to become populated. With the population in these central levels, an EPR spectrum with both absorptive and emissive transitions will arise (Figure 4b).

In general, ENDOR transitions can occur between any pair of eigenstates in the system where (i) there is a nuclear $\alpha \leftrightarrow \beta$ spin flip and (ii) the electronic parts of the eigenstates are nonorthogonal. Consequently, for the radical pair, there are allowed ENDOR transitions between the pure triplet states (i.e., $|1_\alpha\rangle \leftrightarrow |1_\beta\rangle$ and $|4_\alpha\rangle \leftrightarrow |4_\beta\rangle$). These have the same frequencies as the familiar ENDOR transitions arising from the coupling between a single radical and a spin- $1/2$ nucleus (i.e., ω_+ and

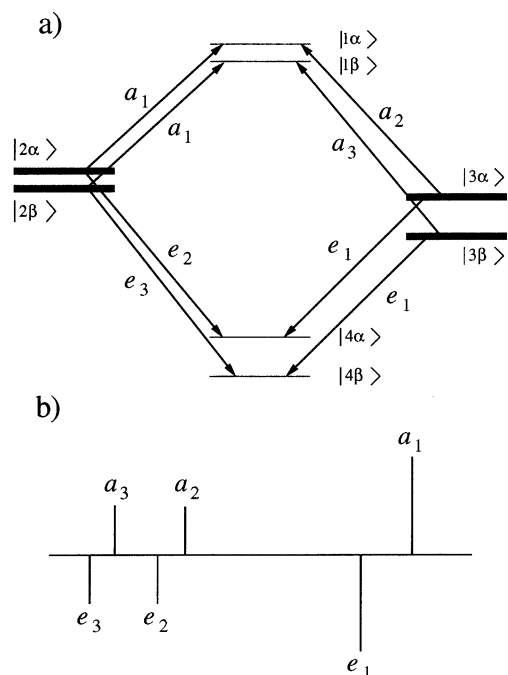


Figure 4. (a) Energy-level diagram for a weakly coupled radical pair according to the model used in these calculations. Only the central four states are populated at the time of the first mw pulse. For this radical pair, six EPR transitions are possible, giving rise to the spectrum shown in (b).

ω_-). In contrast to the single-radical case, however, the four mixed $|S\rangle/|T_0\rangle$ states give rise to up to four additional “partially-allowed” transitions:

$$\begin{aligned} t_1 &= |2_\alpha\rangle \leftrightarrow |2_\beta\rangle & t_3 &= |2_\alpha\rangle \leftrightarrow |3_\beta\rangle \\ t_2 &= |3_\alpha\rangle \leftrightarrow |3_\beta\rangle & t_4 &= |3_\alpha\rangle \leftrightarrow |2_\beta\rangle \end{aligned} \quad (7)$$

Each $|S\rangle/|T_0\rangle$ state has an ENDOR frequency and a transition probability governed not only by the hyperfine coupling but also by the strength of the spin–spin coupling between the electrons.

The polarization in the experimental TR-ENDOR spectra can be explained with the aid of Figures 4 and 5. If the absorptive transition marked a_2 in Figure 4a is excited by a mw pulse, then population is transferred from $|3_\alpha\rangle$ to $|1_\alpha\rangle$, and the population of the energy levels is that shown in Figure 5a. As the radio frequency is varied, three of the six possible ENDOR transitions are selected. The usual low-frequency ENDOR line is seen at $\nu_{\text{RF}} = \omega_+$, and in addition, transitions t_2 and t_3 are also partially allowed. In general, these transitions do not lie at ω_- but are offset from this value as a result of their dependence upon D and J . Because the excited EPR line giving rise to these three transitions is absorptive, each line is absorptive, as indicated in Figure 5b. In principle, because the populations of states $|2_\alpha\rangle$ and $|3_\beta\rangle$ will not be exactly equal, an absorptive ENDOR line resulting from transition t_4 is also possible. This effect is significant only when j and a are of comparable size. Emissive ENDOR lines are seen when an emissive EPR line, such as e_2 in Figure 4, is excited. In this case, three emissive ENDOR lines would be seen at $\nu_{\text{RF}} = \omega_-$, t_1 , and t_4 , with these last two being generally displaced from ω_+ . Additionally, if the populations of $|2_\beta\rangle$ and $|3_\alpha\rangle$ are different, t_3 will give rise to a fourth emissive ENDOR line.

In the situation where the spin–spin coupling is small compared to the inhomogeneous broadening, transitions a_2 and e_2 will be largely overlapping and will both occur within the

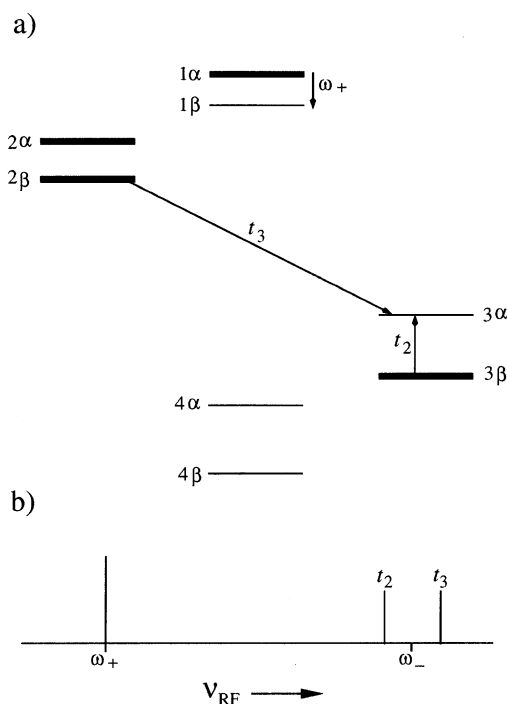


Figure 5. (a) Population of energy levels after a π pulse excites absorptive transition a_2 (see Figure 4) and resulting possible ENDOR transitions ω_- , t_2 , and t_3 . (b) Corresponding ENDOR spectrum.

excitation bandwidth of even selective mw pulses. In this case, all six ENDOR transitions, with t_3 and t_4 being both emissive and absorptive, will be observed. This gives rise to a TR-ENDOR spectrum with both absorptive and emissive parts. The shape of the ENDOR spectrum therefore crucially depends on the relative probabilities of exciting emissive and absorptive EPR transitions with a single mw pulse. This is clearly seen in Figure 3, in which spectra taken at the edges of the FSE, where the FSE is emissive, show mainly emissive transitions. The central region of the FSE is a mixture of emissive and absorptive transitions, which leads to increased absorptive character in the TR-ENDOR traces.

The frequencies of the partially allowed TR-ENDOR transitions introduced in eq 7 come directly from the eigenvalues of the spin Hamiltonian given in eq 2:

$$\begin{aligned} t_1 &= \omega_N - \frac{1}{2}(\Omega_\alpha - \Omega_\beta) & t_3 &= \omega_N - \frac{1}{2}(\Omega_\alpha + \Omega_\beta) \\ t_2 &= \omega_N + \frac{1}{2}(\Omega_\alpha - \Omega_\beta) & t_4 &= \omega_N + \frac{1}{2}(\Omega_\alpha + \Omega_\beta) \end{aligned} \quad (8)$$

For a particular nucleus, the t_i values depend on a , q , and j . For a weakly coupled radical pair, the difference between the Larmor frequencies of the two electrons (q) is far greater than j , the sum of the exchange and dipolar interactions. In this case, the quantity q/j is large and approaches infinity in the limit of weak coupling. Conversely, strongly coupled radical pairs have $|q| \ll |j|$, and in the limit of strong coupling, $q/j \rightarrow 0$. The dependence of the t_i values on q/j can be investigated by fixing j and considering the effect of q on the quantities $(\Omega_\alpha - \Omega_\beta)$ and $(\Omega_\alpha + \Omega_\beta)$. The relationships between the t_i and q in the case where $|a| \gg |j|$ are illustrated by solid lines in Figure 6 and explained below.

As $|q|$ increases beyond $|q| = |a|/2$, $(\Omega_\alpha - \Omega_\beta)$ approaches a , and $(\Omega_\alpha + \Omega_\beta) \rightarrow 2|q|$. This causes t_1 and t_2 to approach ω_+ and ω_- respectively as $q \rightarrow \infty$, and t_3 and t_4 to approach $\pm\infty$ in the same limit. In the region where $|q| < |a|/2$, where the limit

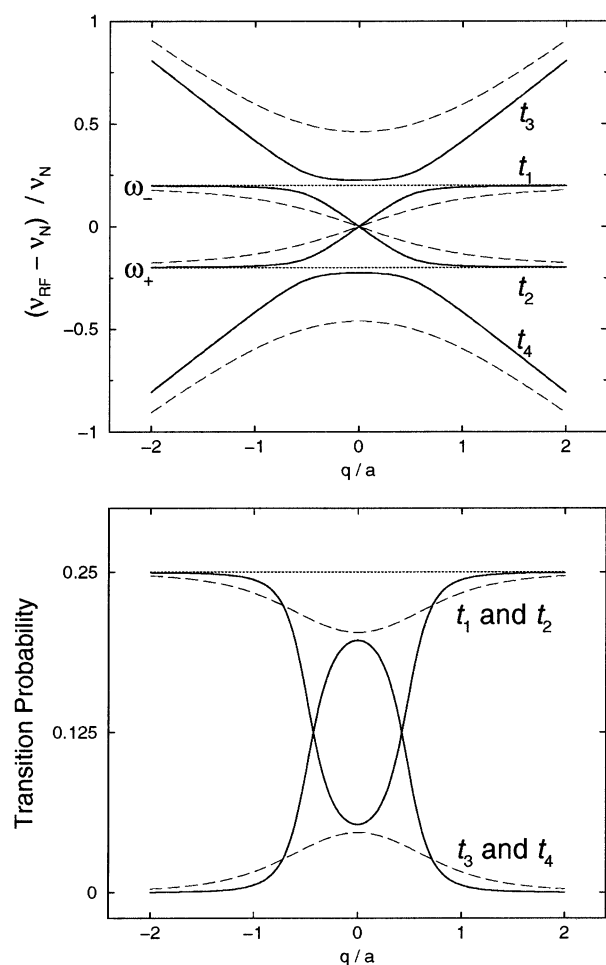


Figure 6. (Top) Dependence of the S/T₀ ENDOR transition frequencies (t_1 ... t_4) on q/a for the RP. (Bottom) Dependence on the transition probabilities of the same transitions. In both, a and j have constant values. (—) $a \gg j$; (---) $j \gg a$.

of strong electronic coupling is approached, $(\Omega_\alpha - \Omega_\beta)$ is proportional to $2q$ so that at the limit $q \rightarrow 0$, t_1 and t_2 are both equal to ω_N . $(\Omega_\alpha + \Omega_\beta)$, however, loses its dependence on $|q|$ as $q \rightarrow 0$ and tends to $\sqrt{a^2 + 4j^2}$ at the limit. The quantity $(\Omega_\alpha + \Omega_\beta)$ is equal to the energy gap between the centers of the nuclear sublevel pairs ($|2_\alpha\rangle/|2_\beta\rangle$) and ($|3_\alpha\rangle/|3_\beta\rangle$), and this last result shows that these pairs will never come closer in energy than this.

At the point at which $q = a/2$, Ω_β is equal to j , and the β -nucleus manifold is at the strong-coupling limit regardless of the size of q/j . That is to say that $|2_\beta\rangle = |S\rangle$ and $|3_\beta\rangle = |T_0\rangle$, and the Larmor frequency of electron A coupled to a β -spin nucleus is equal to that of electron B (which is coupled only to electron A). The eigenvalues lie in different orders on either side of $q = a/2$, leading to the singularity seen in Figure 6. A similar effect is seen in the α -nucleus manifold when $q = -a/2$.

The intensity of each ENDOR transition is equal to the difference in population between states $|j\rangle$ and $|k\rangle$ multiplied by the transition probability³⁶ $|\langle \hat{I}_y \rangle_{jk}|^2$. The transition probabilities of the pure triplet ENDOR transitions are independent of both the spin-spin and hyperfine couplings, and for both, $|\langle \hat{I}_y \rangle_{jk}|^2$ has the value of $1/4$. The transition probabilities for transitions between mixed states are dependent on j , q , and a . When $|q|$ is large, the weak-coupling limit is approached, and states $|2_\alpha\rangle$ and $|2_\beta\rangle$ have electronic character similar to $|\alpha\beta\rangle$ whereas $|3_\alpha\rangle$ and $|3_\beta\rangle$ are $|\beta\alpha\rangle$ -like. Therefore, transitions t_1 and t_2 ($|2_\alpha\rangle \leftrightarrow$

$|2_\beta\rangle$ and $|3_\alpha\rangle \leftrightarrow |3_\beta\rangle$, respectively) are intense whereas t_3 and t_4 , which require both Δm_I and Δm_S to be equal to 1, are very weak. When $|q|$ is small and the strong-coupling limit is approached, $|2_\alpha\rangle$ and $|2_\beta\rangle$ are no longer similar in character, and t_1 is less favored. Likewise, the transition probability of t_2 decreases because $|3_\alpha\rangle$ and $|3_\beta\rangle$ are no longer the same. It follows that the transition probabilities of t_3 and t_4 must both increase in this case. The calculated ENDOR transition probabilities are shown in Figure 6 (bottom).

For $|j| \gg |a|$, the dashed lines in Figure 6 apply. t_1 and t_2 still approach ω_+ and ω_- as $|q|$ increases but do so more gradually. These transitions are considerably more intense for larger j . Transitions t_3 and t_4 are constantly at low intensity when $|j| \gg |a|$. As before, they approach infinity as $|q|$ becomes large and are once again bounded by $\omega_N \pm \sqrt{a^2 + 4j^2}$ as $|q| \rightarrow 0$.

3.2.2. Analysis of Experimental Spectra. The experimental TR-ENDOR spectra shown in Figure 3 can now be further explained. Because the S/T₀ ENDOR transitions are highly dependent upon q , j , and a , they will give rise to very broad low-intensity features in the ENDOR spectrum. In comparison, the fully allowed ENDOR transitions will give sharp lines and be the dominating contribution to the spectral shape. It is therefore unlikely that it would be possible to extract the values of D and J from TR-ENDOR spectra taken from a radical pair such as $P_{700}^+ A_1^-$.

The \mathbf{g} tensor of the quinone A_1^- is defined with g_x and g_y in the plane of the quinone ring and with g_x along the C—O bond. Both of these \mathbf{g} -tensor components are larger than those of P_{700}^+ . This means that at the low-field edge, the FSE is dominated by contributions from molecules with the quinone g_x , and hence the C—O bond, parallel to the field. At the extreme low-field edge of the FSE, the mw pulses excite an emissive EPR transition in these molecules. The theory suggests that the methyl tensor should give a strongly emissive signal on the high-frequency side of the TR-ENDOR spectrum taken at 343.7 mT and a lower-intensity, broader emissive signal on the low-frequency side. In the spectrum, an axial tensor is observed between 19 and 21 MHz. The perpendicular component (a_\perp) is clearer than the parallel component (a_\parallel) because the principal axis of the hfc lies in the molecular plane, roughly along the C—CH₃ bond at about 60° from g_x (see Figure 2). In the TR-ENDOR spectrum taken at 343.7 mT, the tensor on the low-frequency side is badly misshapen, and a small but distinct absorptive signal is seen at a_\parallel . This effect is due to the excitation of a small number of molecules aligned with the quinone g_y axis along the field. ENDOR from this EPR transition gives a strong absorptive signal on the low-frequency side and weaker absorptive signals on the high-frequency side of the TR-ENDOR spectrum.

As the field is increased, ENDOR lines due to the excitation of molecules with the g_y aligned along the field become more prominent, and the low-frequency side of each ENDOR spectrum has greater and greater absorptive character. In addition, because the principal axis of the methyl hfc is aligned close to g_y , a_\parallel becomes clearly visible in the spectra. Beyond the center of the FSE, more molecules with g_z aligned parallel to the field are selected, resulting again in a loss of a_\parallel . Toward the high-field side of the EPR spectrum, the ENDOR spectra are emissive once more and show clear features only on the high-frequency side. Indeed, at the extreme high-field edge, all contributions to the low-frequency part of the methyl tensor are broadened and cancel each other almost completely, as expected from the model.

3.3. Simulation of TR-ENDOR Spectra. Calculations were performed in the rotating frame using standard density matrix methods³⁷ for the pulse sequence

$$\pi_{\text{mw}} - \pi_{\text{RF}} - \frac{\pi}{2}_{\text{mw}} - \tau - \pi_{\text{mw}} - \tau - \text{echo}.$$

The initial density matrix reflects the dephasing of the zero quantum coherence from the singlet state. Evolution of the density matrix during each pulse and during the free-evolution periods ($\tau = 600$ ns) in the detection sequence was taken into account. Pulse amplitudes were $B_1^{\text{mw}} = 0.14$ mT, $\gamma B_1^{\text{mw}}/2\pi = 4$ MHz and $B_1^{\text{RF}} = 0.02$ mT, $\gamma B_1^{\text{RF}}/2\pi = 62.5$ kHz. The pulse durations, chosen to give flip angles π_{mw} and π_{RF} , were 125 and 8000 ns, respectively. In these calculations, only the height of the echo at the end of the pulse sequence was used; an integration over the whole echo was not found to improve the quality of the simulated spectra significantly.

To model the field-swept echo spectrum and field-dependent TR-ENDOR correctly, the full **g** anisotropy of each radical was included. The principal values and orientations of the **g** tensor and the vector describing the orientation of the dipolar coupling (which lies along the g_x axis of the quinone) were those for P_{700}^+ and A_1^- derived from transient EPR.¹⁴ Values of the spin-spin coupling parameters, $D = -4.76$ MHz and $J = 0.03$ MHz, were taken from OOP-ESEEM experiments.³⁸ Hyperfine coupling from a single spin- $1/2$ nucleus is included as an axial tensor with isotropic and anisotropic parts taken from those determined for the A_1^- methyl coupling in PSI (i.e., $a_{\parallel} = 12.8$ MHz and $a_{\perp} = 9.1$ MHz;^{28,29} see Figure 2). The axis of this coupling was set in the xy plane of the quinone at 60° to the C–O bond.

Inhomogeneous broadening on each electron spin was included as a Gaussian distribution of Larmor frequencies; ω_A , representing A_1^- , was distributed over 2.5 G, and ω_B , representing P_{700}^+ , over 6 G. These values were chosen by comparing the experimental and simulated FSE spectra. All experiments were taken in frozen solution, so a powder average was performed by integrating over 1594 different orientations of the B_0 field. Calculations were performed using the EXORCYCLE phase cycle³⁹ on the detection sequence because this dramatically reduced the number of B_0 field orientations needed and consequently saved on computation time. The spectra were calculated at the X-band (9.5 GHz) with $\omega_N = 14.7$ MHz.

Calculated field-swept echo (FSE) and field-dependent TR-ENDOR spectra for the three spin models are shown in Figure 7. A qualitative comparison between this Figure and the experimental results in Figure 3 shows that the FSE reproduces the general E/A/E polarization pattern seen for $P_{700}^+ A_1^-$ but shows some additional resolved structure. This structure arises because the model contains only one spin- $1/2$ nucleus explicitly rather than the three coupled protons of a methyl group. The simulated TR-ENDOR spectra show a field dependence similar to that seen in the experiment. At low magnetic field, the spectra are exclusively emissive, with absorptive ENDOR contributions becoming important on the low-frequency side only after the zero crossing at about 338 mT. Beyond this point, the spectra show both absorptive and emissive contributions until the high-field side of the FSE is reached, where the spectra are purely emissive again and, as seen in the experiment, the low-frequency side of the ENDOR is lower in intensity than the high-frequency side.

In each of the simulated ENDOR spectra, the axial tensor is positioned exactly as expected given the values of a_{\parallel} and a_{\perp} used. If the interaction between the electrons is removed and

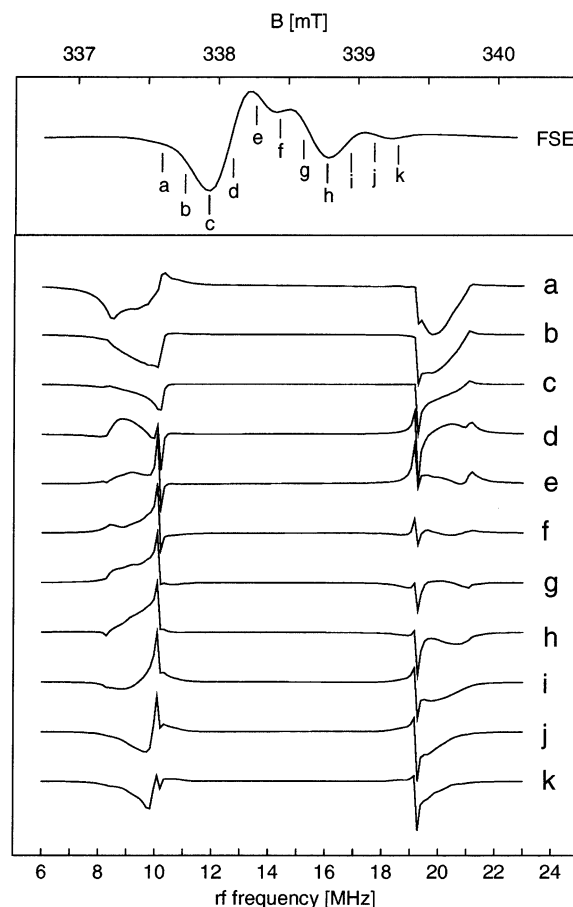


Figure 7. Simulated field-swept echo (top) and TR-ENDOR spectra of $P_{700}^+ A_1^-$.

the simulation is repeated, the axial tensor does not shift. This is in contrast to the effect seen in Figure 2. Here the position of the methyl hfc in the radical-pair spectrum shows a small but distinct shift to smaller coupling compared to the same hfc in the A_1^- spectrum. This is not seen in the simulation, suggesting that the shift is not due to the nature of the TR-ENDOR experiment. To ensure that this effect is not a consequence of the pseudosecular part of the hfc, the model was extended to include this interaction. The resulting ENDOR simulations (data not shown) were identical to those shown in Figure 7. We conclude that the pseudosecular hfc is not responsible for this shift but that it is probably due to small differences in the local geometry within the phyloquinone binding pocket. Photoaccumulation takes place at 205 K, where the protein is still rather mobile. In contrast, $P_{700}^+ A_1^-$ is created at 80 K, at which temperature some degrees of freedom will no longer be accessible and the protein will be unable to reorganize in exactly the same way as it does at higher temperatures.

3.4. Hyperfine Couplings of Different Signs. It is simple to extend the model to include a second spin- $1/2$ nucleus that is also coupled to electron A. We can use this extended model to investigate whether TR-ENDOR on SCRPs can be used to determine the relative signs of hyperfine couplings to the same radical. Figure 8 shows the effect on the spectrum of changing the sign of one of the two hfc's. Because the qualitative shape of powder ENDOR spectra from radical pairs has been discussed above, for clarity, both hfc's are now assumed to be isotropic. Values of the hfc's used are $|a_{\text{iso}}| = 10$ and 5 MHz, respectively. In the top trace, both hfc's are positive and give an A/E pattern. In the lower trace, the smaller hfc has a negative sign, and its

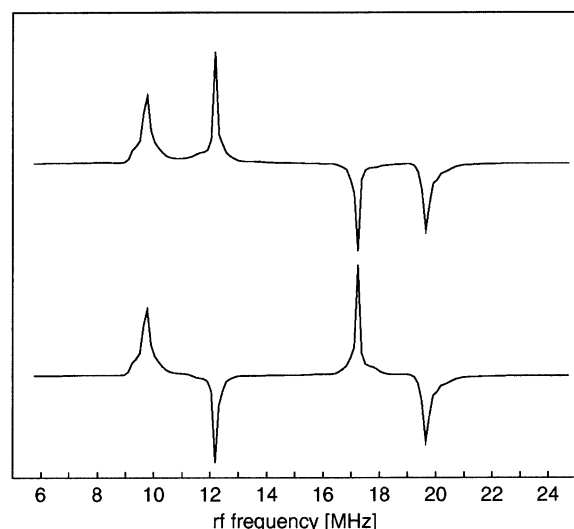


Figure 8. Simulated TR-ENDOR for a radical pair with two spin- $1/2$ hyperfine couplings to the same radical. Both hfcs are assumed to be isotropic. (Top) $a_1 = +10$ MHz and $a_2 = +5$ MHz. (Bottom) $a_1 = +10$ MHz and $a_2 = -5$ MHz.

corresponding ENDOR lines are E/A. This effect is the same as that seen in the TR-ENDOR spectrum shown in Figure 2, with the lines arising from the methyl hfc and those marked *.

Using the theory developed in the previous section, we find that this effect is straightforward to explain. A change in the sign of a affects the energy differences between sublevel pairs. With a negative value of a , $\Delta E_{(1\alpha \leftrightarrow 1\beta)}$ becomes ω_- , and $\Delta E_{(4\alpha \leftrightarrow 4\beta)}$, ω_+ . Similarly, $\Delta E_{(2\alpha \leftrightarrow 2\beta)}$ becomes t_2 , and $\Delta E_{(3\alpha \leftrightarrow 3\beta)}$, t_1 . t_3 and t_4 also interchange. These changes reverse the emissive or absorptive nature of each ENDOR line in the TR-ENDOR spectrum. Figure 8 shows that, provided the hyperfine couplings are sufficiently resolved, it should be possible to determine the relative signs of the hfcs from these spectra without the use of another experiment such as general-TRIPLE.

4. Conclusions

We have presented TR-ENDOR spectra from the SCRPP P_{700}^+ A_1^- in a frozen solution of PSI observed at different resonance fields. The spectra not only are a superposition of the ENDOR spectra expected for the individual radicals P_{700}^+ and A_1^- but are more complicated. Unusually, the TR-ENDOR spectra are composed of both absorptive and emissive contributions, with the quantities of each exhibiting a strong dependence on the magnetic field. Using the theory of spin-correlated radical pairs, we have investigated these observations. Thereby, we have found that the small differences in the positions of pronounced spectral features of A_1^- between stationary and TR-ENDOR experiments are not due to differences in the types of the experiments but are likely caused by differences in the binding pocket of A_1^- between the photoaccumulated and the radical-pair state.

The atypical appearance of the TR-ENDOR spectra is a consequence of the electron-spin polarization and the mixed $|S\rangle$ and $|T_0\rangle$ states within the radical pair. TR-ENDOR lines are absorptive if the EPR line excited by the Davies ENDOR pulse sequence is absorptive and emissive if the EPR line is emissive. The TR-ENDOR spectra shown here are absorptive/emissive because for this radical pair the spin-spin coupling is generally small compared to the inhomogeneous broadening and both absorptive and emissive EPR transitions can be excited simultaneously with the same mw pulse.

The mixed electronic $|S\rangle$ and $|T_0\rangle$ states are the origin of four extra ENDOR transitions in addition to those found at ω_+ and ω_- . The positions and intensities of these ENDOR lines are crucially dependent upon the strength of the dipolar and exchange interaction as well as the size of the hfc. In a weakly coupled radical pair such as P_{700}^+ A_1^- in PSI, it is unlikely that these extra transitions will have a large effect on the TR-ENDOR spectrum. TR-ENDOR is also shown to be capable of distinguishing between hyperfine couplings with different signs. If the TR-ENDOR experiment were applied to single-crystal samples of P_{700}^+ A_1^- in PSI, it could, in principle, provide information about A_1^- that currently cannot be obtained from conventional ENDOR studies on the photoaccumulated radical.

Acknowledgment. We thank Professor W. Lubitz (Berlin/Mülheim) for generous support and encouragement and Dr. C. W. M. Kay (Berlin) for helpful discussion. We are grateful to Dr. P. J. Hore (Oxford) for making available his SCRPP-ESEEM simulation program. This work was supported by the Deutsche Forschungsgemeinschaft (Sfb 498 TP C5) and a grant from the European Commission under its Training and Mobility of Researchers program (FMRX-CT98-0214).

References and Notes

- (1) Jordan, P.; Fromme, P.; Witt, H. T.; Klukas, O.; Saenger, W.; Krauss, N. *Nature (London)* **2001**, *411*, 909.
- (2) Brettel, K.; Leibl, W. *Biochim. Biophys. Acta* **2001**, *1507*, 100.
- (3) Webber, A. N.; Lubitz, W. *Biochim. Biophys. Acta* **2001**, *1507*, 61.
- (4) Vassiliev, I. R.; Antonkine, M. L.; Golbeck, J. H. *Biochim. Biophys. Acta* **2001**, *1507*, 139.
- (5) Deligiannakis, Y.; Rutherford, A. W. *Biochim. Biophys. Acta* **2001**, *1507*, 226.
- (6) Rigby, S. E. J.; Evans, M. C. W.; Heathcote, P. *Biochim. Biophys. Acta* **2001**, *1507*, 247.
- (7) Schlodder, E.; Falkenberg, K.; Gergeleit, M.; Brettel, K. *Biochemistry* **1998**, *37*, 9466.
- (8) van der Est, A. *Biochim. Biophys. Acta* **2001**, *1507*, 212.
- (9) Salikhov, K. M.; Kandrashkin, Y. E.; Salikhov, A. K. *Appl. Magn. Reson.* **1992**, *3*, 199.
- (10) Tang, J.; Thurnauer, M. C.; Norris, J. R. *Chem. Phys. Lett.* **1994**, *219*, 283.
- (11) Dzuba, S. A.; Gast, P.; Hoff, A. J. *Chem. Phys. Lett.* **1995**, *236*, 595.
- (12) Bittl, R.; Zech, S. G. *Biochim. Biophys. Acta* **2001**, *1507*, 194.
- (13) Bittl, R.; Zech, S. G.; Fromme, P.; Witt, H. T.; Lubitz, W. *Biochemistry* **1997**, *36*, 12001.
- (14) Zech, S. G.; Hofbauer, W.; Kamlowski, A.; Fromme, P.; Stehlik, D.; Lubitz, W.; Bittl, R. *J. Phys. Chem. B* **2000**, *104*, 9728.
- (15) Käss, H.; Fromme, P.; Witt, H.; Lubitz, W. *J. Phys. Chem. B* **2001**, *105*, 1225.
- (16) Bittl, R.; Zech, S. G.; Teutloff, C.; Krabben, L.; Lubitz, W. In *Photosynthesis: Mechanisms and Effects*; Garab, G., Ed.; Kluwer: Dordrecht, The Netherlands, 1998; Vol. I, pp 509.
- (17) Zybailov, B.; van der Est, A.; Zech, S. G.; Teutloff, C.; Johnson, T. W.; Shen, G.; Bittl, R.; Stehlik, D.; Chitnis, P. R.; Golbeck, J. H. *J. Biol. Chem.* **2000**, *275*, 8531.
- (18) Buckley, C. D.; Hunter, D. A.; Hore, P. J.; McLauchlan, K. A. *Chem. Phys. Lett.* **1987**, *135*, 307.
- (19) Closs, G. L.; Forbes, M. D. E.; Norris, J. R. *J. Phys. Chem.* **1987**, *91*, 3592.
- (20) Stehlik, D.; Bock, C. H.; Petersen, J. *J. Phys. Chem.* **1989**, *93*, 1612.
- (21) Fromme, P.; Witt, H. T. *Biochim. Biophys. Acta* **1998**, *1365*, 175.
- (22) Hore, P.; Hunter, D. A.; McKie, C. D.; Hoff, A. J. *Chem. Phys. Lett.* **1987**, *137*, 495.
- (23) Bittl, R.; Kothe, G. *Chem. Phys. Lett.* **1991**, *177*, 547.
- (24) Kothe, G.; Weber, S.; Bittl, R.; Ohmes, E.; Thurnauer, M. C.; Norris, J. R. *Chem. Phys. Lett.* **1991**, *186*, 474.
- (25) Kothe, G.; Weber, S.; Ohmes, E.; Thurnauer, M. C.; Norris, J. R. *J. Phys. Chem.* **1994**, *98*, 2706.
- (26) Dzuba, S. A.; Bosch, M. K.; Hoff, A. J. *Chem. Phys. Lett.* **1996**, *248*, 427.
- (27) Davies, E. R. *Phys. Lett. A* **1974**, *47*, 1.

- (28) Rigby, S. E. J.; Evans, M. C. W.; Heathcote, P. *Biochemistry* **1996**, 35, 6651.
- (29) Teutloff, C.; MacMillan, F.; Bittl, R.; Lendzian, F.; Lubitz, W. In *Photosynthesis: Mechanisms and Effects*; Garab, G., Ed.; Kluwer: Dordrecht, The Netherlands, 1998; Vol. I, pp 607.
- (30) Teutloff, C.; Hofbauer, W.; Zech, S. G.; Stein, M.; Bittl, R.; Lubitz, W. *Appl. Magn. Reson.* **2001**, 21, 363.
- (31) Möbius, K.; Plato, M.; Lubitz, W. *Phys. Rep.* **1982**, 87, 171.
- (32) Hore, P. J. In *Advanced EPR: Applications in Biology and Biochemistry*; Hoff, A. J., Ed.; Elsevier Science Publishing Company: Amsterdam, 1989; p 405.
- (33) Weber, S.; Kothe, G.; Norris, J. R. *J. Chem. Phys.* **1997**, 106, 6248.
- (34) Timmel, C. R.; Fursman, C. E.; Hoff, A. J.; Hore, P. J. *Chem. Phys.* **1998**, 226, 271.
- (35) Jeschke, G. *J. Chem. Phys.* **1997**, 106, 10072.
- (36) Abragam, A. *The Principles of Nuclear Magnetism*; Oxford University Press: Oxford, U.K., 1961; p 28.
- (37) Ernst, R. R.; Bodenhausen, G.; Wokaun, A. *Principles of Nuclear Magnetic Resonance in One and Two Dimensions*; Clarendon Press: Oxford, U.K., 1987.
- (38) Zech, S. G.; Lubitz, W.; Bittl, R. *Ber. Bunsen-Ges. Phys. Chem.* **1996**, 100, 2041.
- (39) Bodenhausen, G.; Freeman, R.; Turner, D. L. *J. Magn. Reson.* **1977**, 27, 511.